TITLE PAGE

Title: Analysis of the main geometrical characteristics that affect the bonding of ribs in rebars thinly covered to repair masonry structures

Author names and affiliations:

Esperanza Rodriguez-Mayorga[a]

Beatriz Hortigon[b]

Fernando Ancio[b]

[a]Department of Estructuras de Edificación e Ingeniería del Terreno. Escuela Técnica Superior de Arquitectura. Universidad de Sevilla. Reina Mercedes 2. 41012. Spain. espe@us.es

[b]Department of Mecánica de Medios Continuos y Teoría de Estructuras. Escuela Politécnica Superior. Universidad de Sevilla. Virgen de África 7. 41011. Spain. bhortigon@us.es

[b]Department of Mecánica de Medios Continuos y Teoría de Estructuras. Escuela Politécnica Superior. Universidad de Sevilla. Virgen de África 7. 41011. Spain. ancio@us.es

Corresponding autor: Esperanza Rodriguez-Mayorga (espe@us.es)

Highlights

Bonding in 5-mm stainless-steel rebars embedded in a hydraulic medium is analysed

Microplane theory reproduces behaviour of a hydraulic medium in Finite Element Method

Bonding is evaluated by Finite Element Method defining a Cohesive Zone Model

Multi-linear regression enables results to be extended over a larger set of samples

The most influential geometric features of ribs in bonding behaviour are ascertained

Abstract

The use of stainless steel rebars in the repair of masonry structures is widespread and has traditionally produced excellent results. In these cases, rebars usually present diameters of below 8 mm covered with thin layers of mortar or grout. Research is necessary to characterise bonding under these particular conditions, hitherto unavailable.

In this research, the geometry of ribs is parameterised and later analysed through the Finite Element Method. To this end, the Microplane model and Cohesive zone model are employed. Based on the numerical results, the geometrical aspects of the ribs that mostly affect bonding are identified and discussed.

Graphical abstract

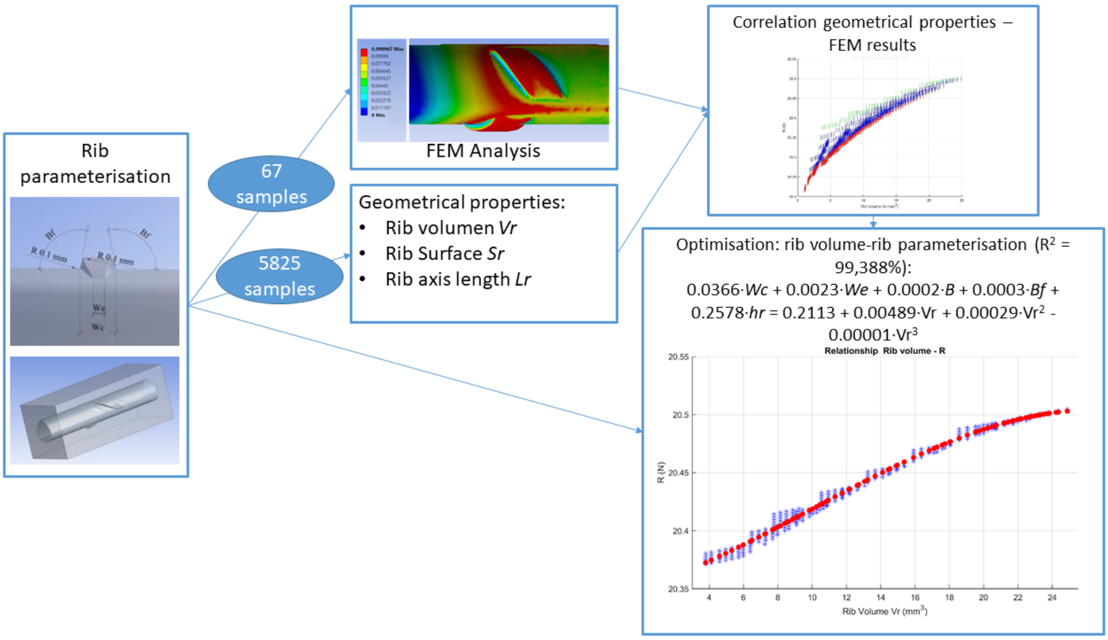

Keywords: masonry repair; stainless-steel rebars; rib shape; bonding; geometrical parameterisation; FEM analysis; microplane model; cohesive zone model; rib optimisation; multilinear regression analysis

Abbreviations

Wc: Central rib width

We: Rib width at the extremities

hr: Rib height

Bf: Rib face angle

B: Angle between rebar and rib axes

Vr: Rib volume

Sr: Rib external surface

Lr: Rib axis length

R: Force transmitted from the sample to the medium that surrounds it

1 Introduction

The repair of masonry has become a major concern in many countries, especially in those rich in vernacular architecture. Masonry has traditionally been used in construction, in huge historic buildings and small humble historical dwellings alike. Historical masonries usually present low resistance and are especially sensitive to damp, mainly due to the high percentage of pores and voids that the system includes, caused by porosity of the components, or by degradation suffered over time. In addition, historical buildings are often affected by rising damp. Damp is one of the main agents of degradation of masonries and can lead buildings to conditions close to collapse due to the reduction of mechanical properties that it causes [1]. In short, it can be stated that masonry is prone to be weakened over time. For this reason, research into reinforcement and repair techniques for masonry is important in areas where this method of construction is abundant.

Several techniques are employed to repair masonry buildings [2–7], among which the transversal tying of walls and bed-joint structural repointing constitute two of the most efficient techniques [8,9]. In both traditional and new masonry structures, these techniques have been widely used and tested and quality results have been attained. Furthermore, when dealing with historical masonry walls, which are usually composed of three leaves infilled with rubble masonry, the effects of tying the external leaves are especially favourable in terms of preventing the instability of layers [10]. Although steel rebars have customarily been used to this end, polymeric fibres have been launched onto the market, and are replacing rebars in popularity [4,11,12]. Fibres exhibit major advantages, principally in terms of the small sections that are commonly required when employed in this context, and that make them the first choice when dealing with heritage. On the other hand, steel rebars are a competitive choice since, depending on the market, are a cheaper option even when stainless steel is chosen for repairs in which rising damp is present [13].

The use of steel rebars to repair masonry is usually carried out by means of introducing rebars between masonry pieces, which gives rise to the repair technique known as bed-joint repointing. This technique has several features: (i) only small diameters can be used; (ii) these rebars must be embedded in mortar or grout, never in concrete; and (iii) the thickness of rebar covering is usually less than 20 mm. These determining factors strongly influence major aspects, such as bonding [14]. Bonding in small diameters under these circumstances has been poorly documented.

Currently, most codes refer to bonding with a parameter called relative rib area (denoted R_r or f_R, depending on the code) which can alternatively be defined as [15,16]:

$$\mathrm{Rr} = \frac{A_r}{d_r \cdot \pi \cdot s_r} \sim 0.8\ to\ 0.9\ \frac{h_r}{s_r} \qquad \text{[Eq. 1]}$$

where:

- A_r: Rib area projected on a plane normal to the rebar axis
- s_r: Spacing between ribs
- h_r: Height of ribs
- d_r: Nominal diameter

Being relative rib area recommended to be greater than 0.035 for diameters from 5 to 6 mm [16].

On the other hand, [17,18] deal with bonding through the geometry of rebars, whose main limitations involve: (i) spacing between consecutive ribs; (ii) angle between rib axis and rebar axis; (iii) rib height; (iv) rib face angle; and (v) the total sum of the gaps between ribs in a transversal section of the rebar. An independent range is set for all these values, with no relationships between them.

There is scarce documentation regarding research into rebars with small diameters. Most authors deal with rebars whose diameters are greater than 8 mm, and especially above 12 mm, and always embedded in concrete. These studies exhibit the importance of Rr as a factor to measure bonding [19–21]. In general, rib height is concluded as the most influential geometrical factor [22,23], together with the resistance of the medium that surrounds the rebar: higher resistances improve bonding stress [24,25]. Although spacing is a geometrical characteristic of the rebar and not of the rib, it should be borne in mind that it stands among the most influential parameters in bonding [22,26]. In contrast, the angle between the rib and the rebar axes remains among the least influential parameters [27]. Finally, bonding stress is strongly influenced by the diameter of the rebar [22], whereby a different behaviour for diameters lower than 8 mm is found by the very few examples of documented research that deal with these values [28]. The extensive use of these small-diameter rebars to reinforce masonries justifies the in-depth study of their particular bonding behaviour.

To conclude this section, it can be stated that small-diameter rebars with thin coverings need special characterisation. Currently, the geometry of rebars with diameters smaller than 8 mm is simply the scaled-down image of rebars with larger diameters, thereby disregarding any special analysis that may be required due to their size. This paper is targeted to research the bonding behaviour of rebars of 5 mm diameter embedded in prisms of dimensions 12x12x30 mm^3 made of hydraulic material in which three of the longitudinal prism faces are fixed. These boundary conditions are set in place in order to reproduce the behaviour of rebars employed in repointing masonry joints, which are confined into a small space between masonry pieces where the displacement of three of the four longitudinal faces of the prism are totally blocked.

The principal objective of the analysis is to identify geometrical characteristics of the rib that most affects the bonding when subject to these particular boundary conditions. Moreover, the possible combinations of geometrical characteristics that could influence bonding have also been researched. Hence, spacing between ribs has not been taken into account so that the effect of parameters external to exclusively rib geometry can be prevented, especially since the influence of spacing is thoroughly recognised. To this end, rebars with only one rib per rebar face, which henceforth will be called samples, are included in this research. The analysis of the samples is carried out by means of Finite Element Analysis (Section 3) and regression analysis (Section 4). Finally, a discussion (Section 5) is included and several conclusions in terms of rib shape optimisation are outlined (Section 6).

2 Materials and methods

The shape of samples analysed in this research is based on the particular geometry of stainless steel rebars with 5 mm nominal diameter. Samples are embedded in the centre of prisms of a 12x12 mm cross-section that simulate the hydraulic medium surrounding the rebars. Both samples and prisms are 30 mm in length, although, to prevent distorting results in the extremities of the sample, only the central length of 26 mm has been considered in contact [15]. The bonding behaviour of the sample inside the rebar is measured in this research by means of the force transmitted from the samples to the prisms when they are longitudinally displaced a fixed quantity. The displacement is applied to one of the transversal faces of the sample.

The process of modelling samples is carried out by means of Rhino V.6 software. Rhino is a 3D modeller that includes Grasshopper among its tools. Grasshopper is a powerful parameterisation software that has been used in this work to generate all the models and subsequently obtain their geometric properties (rib volume, rib surface, rib length): this is tackled in Section 4. Additionally, the open-licenced plug-in known as Anemone, which enables loops to be created in Grasshopper, has facilitated access to the huge number of samples that have been developed for this research (Fig. 1).

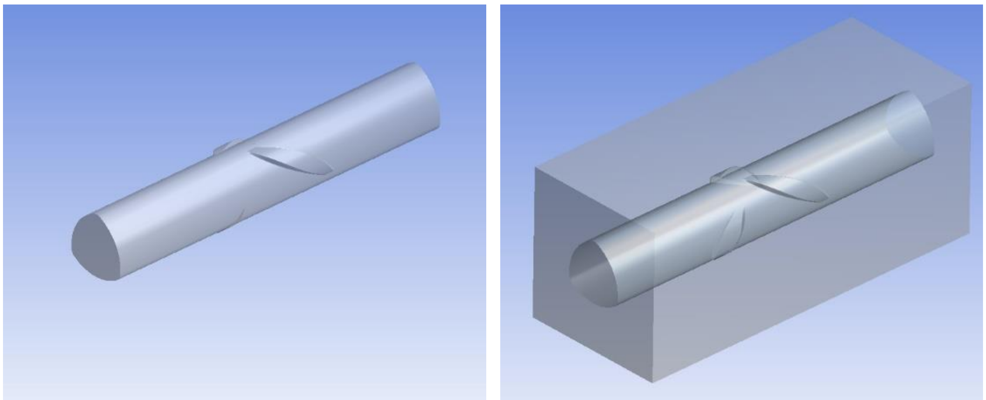

Fig. 1. One of the 67 samples studied in the research: isolated (left-hand side) and embedded in the hydraulic medium (right-hand side).

Samples are composed of a central core where a rib is attached on each face, resulting in 3 ribs per sample in total. In order to minimize the influence that friction core-prism exerts in bonding, and since there is only a rib per core face, samples length is fixed in 30 mm [29,30]. In this way, the effect of different rib shapes in bonding will be more easily identified.

The core of the samples comprises three arcs with filleted corners. Rib designs respond to loft surfaces with trapezoidal transversal section. The parameters employed to control the rib shape include: *Wc,* rib central width, measured in the direction parallel to the rebar axis; *We,* rib width at the extremities, measured in the direction parallel to the rebar axis; *B,* angle between the rib and the rebar axes; *Bf,* rib face angle; and *hr,* height of the rib at its centre. All the ribs are attached to the core and occupy 90% of the length of each core face. The radius on the root (*r*) is established as 0.1 mm. Figure 2 depicts the parameterisation of the samples.

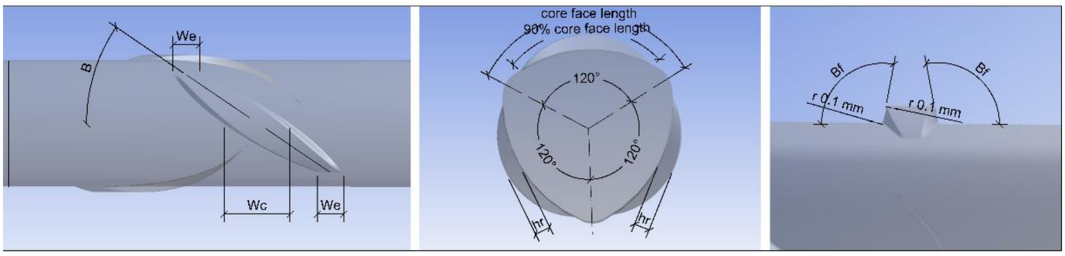

Fig. 2. Parameterisation of the samples in the research.

The values *B*, *Bf*, and *hr* have been set up within the ranges established by the codes [15,17,18]: *B*, from 35º to 75º; *Bf*, from 45º to 90º; *hr*, from 0.15 mm to 0.75 mm. The central width and those at the extremities are not covered by the codes, and therefore, in this research, values ranging from 1 to 4 mm are considered for *Wc* and *We*. The values of all five parameters are combined in two sets of models. In the first set, only one parameter ranges between the lower and upper values, while the other parameters are fixed at a medium value. In the second set, all values range simultaneously. In total, 67 models are analysed by FEM, with 40 models in the first set and 27 in the second. Combinations of values are discussed in Section 4 (Table 1).

3 Calculations

The solid models generated as specified in Section 2 are then imported in ANSYS R.19.3. This Finite Element software is employed to simulate the slippage of the rebar inside the medium under an axial load. Plastic calculations with a cohesive zone model are carried out in order to characterise the behaviour in terms of the bonding of the 67 solid models. These models aim to reproduce the behaviour of the sample embedded in a quasi-brittle medium, such as mortar or grout. Samples of the solid models are automatically generated as explained in Section 2. Surrounding the samples, prismatic blocks of 12x12x30 mm^3 are disposed. In order to reproduce the behaviour of the rebar embedded in the hydraulic infilled between two masonry units, only three of the four longitudinal faces are fixed.

However, the models include two different materials: steel for the samples, and hydraulic material for the surrounding prism. To this end, 8-node Solid185 elements are utilised to model samples. Solid185 elements have three degrees of freedom at each node. Steel has been defined as an isotropic elastic linear material with E=210 GPa and Poisson modulus υ=0.3. No multi-linear stress-strain curve is modelled herein since steel would always operate below yield strength in this research [31,32].

In contrast, materials such as mortars and grouts, exhibit non-linear stress-strain relations with brittle cracking. Regarding tensile strength, sudden softening occurs accompanied by reduction in the stiffness, while in compressive strength, stress-strain behaviour firstly involves ductile hardening followed by softening and reduction in the stiffness. These materials are commonly referred to as quasi-brittle materials. The Microplane model is especially suitable for the characterisation of the behaviour of quasi-brittle materials [33–36]. Based on Mohr's theories regarding the characterisation of materials on various planes, the Microplane model was developed [37–41]. This enables the incorporation of the consideration of continuous damage models on a specific number of planes, known as microplanes. This model was subsequently generalised for both tensile and compressive damage [33,34]. The application of microplanes to elasto-plastic models was later discussed in [42]. Finally, kinematic constraint was adopted since it enables a more stable response during strain softening, preventing, this way, instability in post-peak post-softening damage. The hydraulic material has been thus modelled using 8-node Solid185 elements. Solid185 elements present plasticity, stress stiffening, large deflection, and large strain capabilities, as well as three degrees of freedom at each node, and supports the Elastic Microplane model with damage. This model is suitable for predominantly static load applications, since they are capable of capturing the behaviour of quasi-brittle materials accurately. Microplane model is defined in the software ANSYS though 6 constants, namely C constants. The Microplane constants *C1*, *C2*, and *C3* depend on the compressive strength (*fc*), tensile strength (*ft*), and Poisson's ratio (ν) of the material, and are respectively consistent with the values k_0, k_1, and k_2 in the Microplane theory:

$$k_0 = k_1 = \frac{k-1}{2k(1-2\nu)} \qquad \text{[Eq. 2]}$$

$$k_2 = \frac{3}{k(1+\nu)^2} \qquad \text{[Eq. 3]}$$

where:

$$k = \frac{fc}{ft} \qquad \text{[Eq. 4]}$$

On the other hand, Microplane constants *C4*, *C5*, and *C6* coincide with the values, γ_0^{mic} (equivalent strain energy when the damage to the material starts), α^{mic} (maximum degradation), and β^{mic} (damage evolution rate) in the Microplane theory. The law of damage evolution d^{mic} , as well as the equivalent strain energy at each point according to its macroscopic strain state η^{mic}, link these parameters among them [43–46]:

$$d^{mic} = 1 - \frac{\gamma_0^{mic}}{\eta^{mic}}\left[1 - \alpha^{mic} + \alpha^{mic} \cdot exp\left(\beta^{mic}\left(\gamma_0^{mic} - \eta^{mic}\right)\right)\right] \qquad \text{[Eq. 5]}$$

and are also related with [47]:

$$\eta^{mic} = k_0 \cdot I_1 + \sqrt{k_1^2 \cdot I_1^2 + k_2 \cdot J_2} \qquad \text{[Eq. 6]}$$

Where I_1 and J_2 are the first invariant of the strain tensor and the second invariant of the deviatoric part of the strain tensor ε respectively:

$$I_1 = \varepsilon_1 + \varepsilon_2 + \varepsilon_3 \qquad \text{[Eq. 7]}$$

$$J_2 = 1/6[(\varepsilon_1 + \varepsilon_2)^2 + (\varepsilon_2 + \varepsilon_3)^2 + (\varepsilon_3 + \varepsilon_1)^2] \qquad \text{[Eq. 8]}$$

Finally, the values of *C1*, *C2*, *C3*, *C4*, *C5*, and *C6* are set as 0.729, 0.729, 0.26, 6e-05, 0.75, and 100. In accordance with the mechanical properties of repairing mortars and previous experiences [2,14,47,48]. The coefficients *C1*, *C2* y *C3* respond to the rate f_c / f_t = 8/1=8. The reproduction of some laboratory tests by FE defining MPlane by the coefficients C1, C2, C3, C4, C5 and C6 and the comparison of the experimental and numerical stress-strain curves for them reflects that these coefficients produce acceptable results when modelling repairing mortars. This way, it can be concluded that the use of these coefficients in calculations guarantees the reliability of the obtained results [14,49].

The interface between rebars and grout is defined as a Cohesive Zone Model (CZM) with a mixed debonding interface mode [50,51]. The CZM is able to numerically reproduce the cohesive forces that appear when materials are separated that mainly arise from: (i) friction, due to the joint action of the dilation slip and the shear failure of the grout [52]; and (ii) mechanical interlock, depending on the rib shape and rib separation [26]. Chemical adhesion between mortars and rebars is usually disregarded due to its low influence in bonding [53]. The CZM is modelled through elements CONTA174 and TARGE170.

The CZM in the model is calibrated by means of 10 calculations, where the maximum normal tensile contact stress and maximum equivalent shear contact stress range from 0.1 to 50 MPa. On the contrary, normal compressive stress is not limited by CZM, but by the MPlane definition. The results are evaluated by means of *R*, where *R* is the force transmitted from a sample to the medium that surrounds it when $5 \cdot 10^{-5}$ mm of longitudinal displacement is imposed on one of the transversal faces of the sample.

The main conclusions obtained from this sensitivity analyses (Fig. 3) include: (i) when maximum stresses are set below 0.1 MPa, then forces are poorly transmitted and no convergence is achieved; (ii) when maximum stresses exceed 0.5 MPa, then bonding works perfectly and any failure is initiated by hydraulic material; (iii) when maximum normal and shear stresses range from 0.1 to 0.5 MPa, then failure is defined by bonding, thereby rendering the results highly dependent on changes in the maximum allowable stresses. Stress analysis of rib surface in this last choice verifies that the failure of the contact is caused by shear stresses. In order to enter further in depth in this aspect, maximum stresses for shear and normal tensile contact stresses have been set at 0.10 MPa and 1 MPa, respectively, in the CZM. Reducing shear contact stress as far as possible eases the process of identifying the influence of rib geometrical parameters in bonding, since bonding behaviour is almost totally entrusted to the rib shape. All calculations in this research have been carried out based on these values of maximum shear contact stress and normal tensile contact stress.

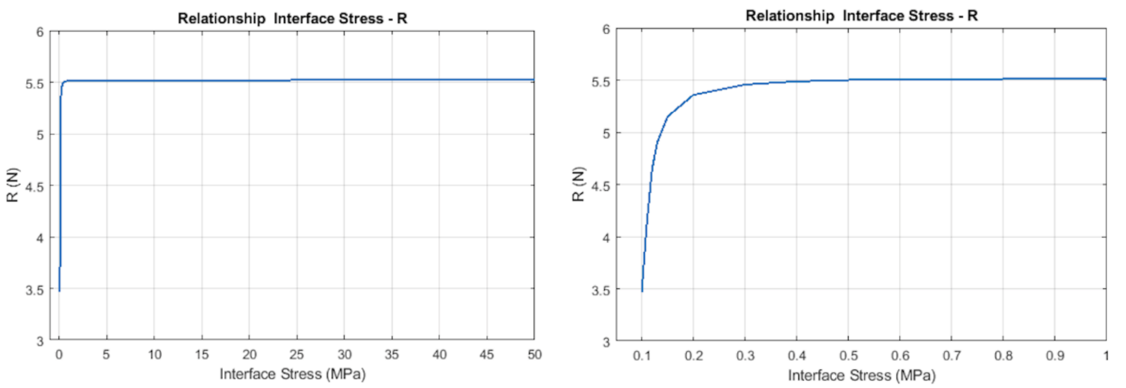

Fig. 3. Results of *R* (force transmitted from sample to the prism) caused by up to $5 \cdot 10^{-5}$ mm of longitudinal displacement of one of the faces of the sample numbered 36 (*Wc*, 2.5 mm; *We*, 2.0 mm; *B*, 35^0; *Bf*, 67.5^0; *hr*, 0.45 mm) with maximum normal tensile and shear contact stresses ranging from 0.1 to 50 MPa (left-hand side) and from 0.1 to 1 MPa (right-hand side).

The sample number 4 (see Table 1 in Section 4), in which all geometrical parameters are fixed at medium values (*Wc*, 2.5 mm; *We*, 2.5 mm; *B*, 35º; *Bf*, 67.7º; *hr*, 45 mm) has been analysed up to failure (Fig. 4). In this analysis, displacement and force R transmitted to the medium have reached $1.65 \cdot 10^{-4}$ mm and 21.459 N respectively. Figure 4 depicts value of force *R* as a function of the displacement applied per load step. This curve shows clearly the sliding failure once the force *R* decreases. Stresses have been analysed in 5 intermediate steps: (i) when R reaches 50% of its maximum value; (ii) when R reaches 75% of its maximum value; (iii) when R reaches its maximum value; (iv) once sliding has occurs; and (v) when R reaches its final value. These five intermediate steps are shown in Figure 4 as A, B, C, D and E respectively.

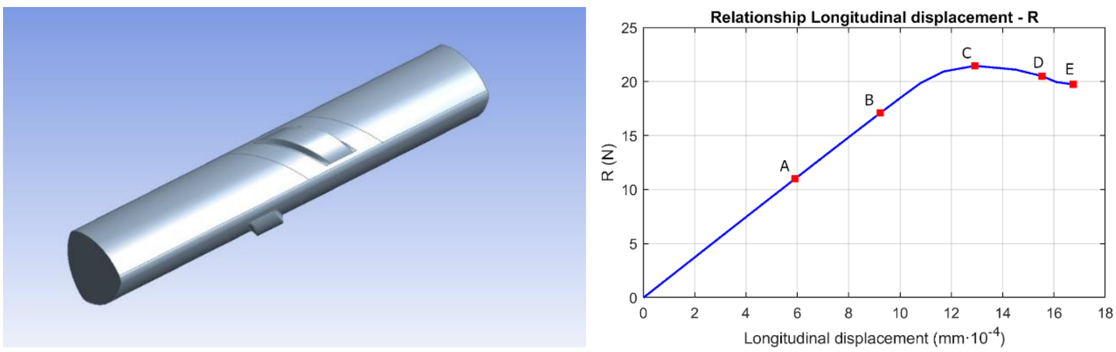

Fig. 4. Sample numbered 4: Wc, 2.5 mm; We, 2.5 mm; B, 35º; Bf, 67.5º; hr, 0.45 mm (left hand side) and chart depicting the force R (N) transmitted to the hydraulic medium as a function of the longitudinal displacement of the sample (right hand side): A, intermediate step in which R reaches 50% of its maximum value; B, intermediate step in which R reaches 75% of its maximum value; C, intermediate step in which R reaches its maximum value; D, intermediate step in which the sample is sliding; and E, intermediate step in which R reaches its final value.

Figure 5 represents the evolution of shear contact stress in the CZM though the 5 intermediate load steps named A to E. The maximum possible value of shear contact stress is 0.1 MPa as has been exposed before. Initially (Figs. 5a and Fig 5b), maximum shear contact stresses are concentrated in the area close to the application of the displacement. Once the maximum force R have been reached (Fig. 5c), a bigger area of the sample is working at the maximum and sliding has occurred in some parts of the sample. Later, damage progresses up to total failure (Figs. 5d and 5e). To enable the analysis in this research of a broad spectrum of rib shapes, only displacements that assure convergence of all models have been imposed to samples. The value of longitudinal displacements applied to all samples have been fixed in $1.1 \cdot 10^{-4}$ mm. This way, although not all samples have been carried up to failure, the situation is quite close to failure. Results obtained for all samples are comparable among them since all have been obtained by applying the same value of displacement.

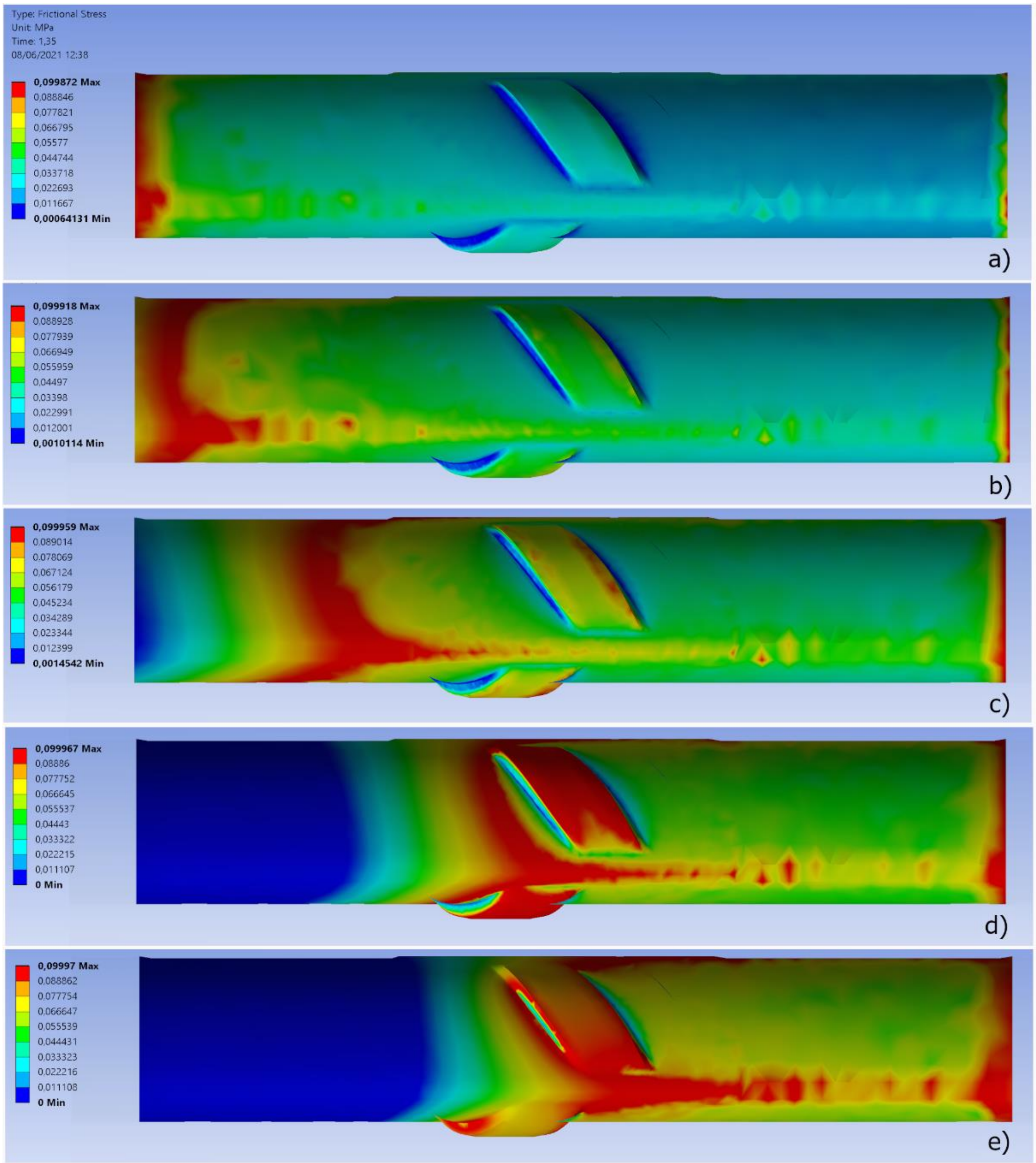

Fig. 5. Shear contact stress in the sample 4 (Wc, 2.5 mm; We, 2.5 mm; B, 35º; Bf, 67.5º; hr, 0.45 mm) when: (a) *R* reaches 50% of its maximum value; (b) *R* reaches 75% of its maximum value; (c) *R* reaches its maximum value; (d) the sample is sliding; (e) *R* reaches its final value.

The set composed by the medium modelled by MPlane, the steel bar, and the contact between them, modelled by CZM were definitely validated altogether through the exactly reproduction of the pull-out tests of a low-diameter reinforcing bar [54]. The tested bar has 8 mm of diameter and is embedded in mortar subjected to 0,50 MPa as confinement pressure (Fig. 6). A displacement in the frontal face of the bar reproduces the force applied in the test. The coefficients describing MPlane were adapted to the materials used in these tests (*k*, 8.67; k_0, *0.737;* k_1, *0.737 and* k_2, *0.24),* with basis on Equations 2, 3 and 4. The maximum value achieved in the FEM simulation was 6252 N, that compared with the value of 6300 N obtained in these tests, confirms the accuracy of the model to be used for this research.

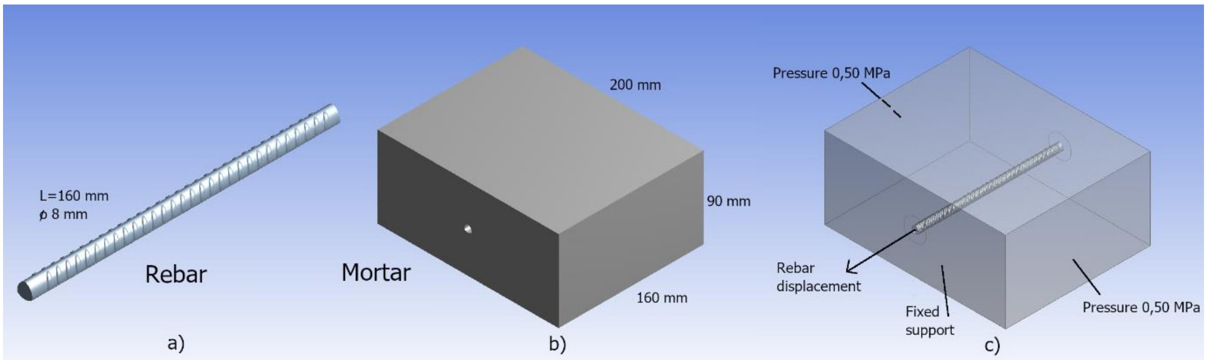

Fig. 6. Reproduction by FEM of a pull-out test: (a) Reinforcing bar with 8 mm diameter and 160 mm length; (b) Mortar block which measurements are 200x160x90 mm; (c) Boundary conditions applied to FEM simulation of the pull-out test.

The shear contact stress distribution for different stages of the FEM simulation of the test are in Figure 7. The maximum values for shear contact stress are attained in areas close to frontal face to the end of the bar whenever the applied force R ranges from the beginning of the simulation to its final value (5%, 20%, 80% and 100% of Rmax, in Figure 7a, 7b, 7c and 7d respectively). In the final stage of the FEM simulation, slipping of the bar can be observed thought zero or almost zero values of shear contact stress, as has also been previously described in Figure 5. Once slippage has occurred, load transmission can only be possible though normal contact stresses developed in rib faces, what finally leads to failure (Fig. 8).

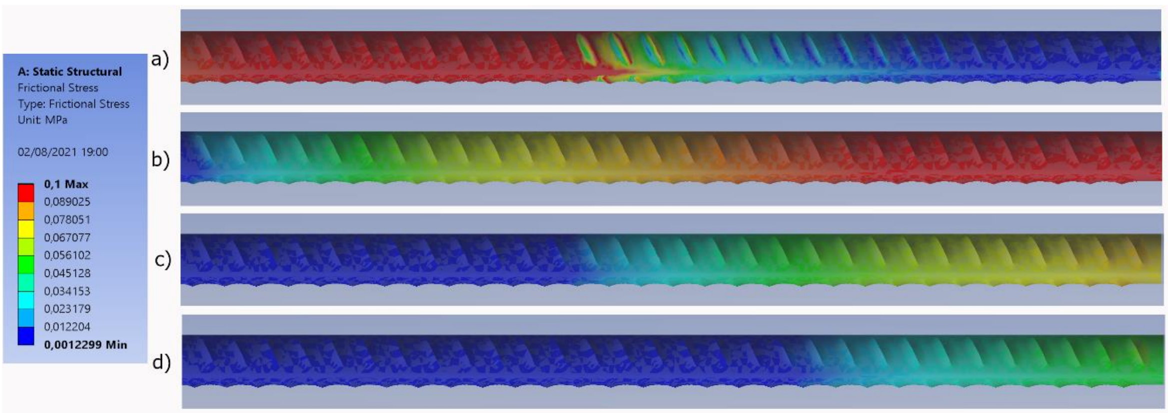

Fig. 7. Shear contact stress in the reinforcing bar when (a) R reaches 5% of its maximum value; (b) R reaches 20% of its final value; (c) R reaches 80% of its final value and (d) R reaches its final value.

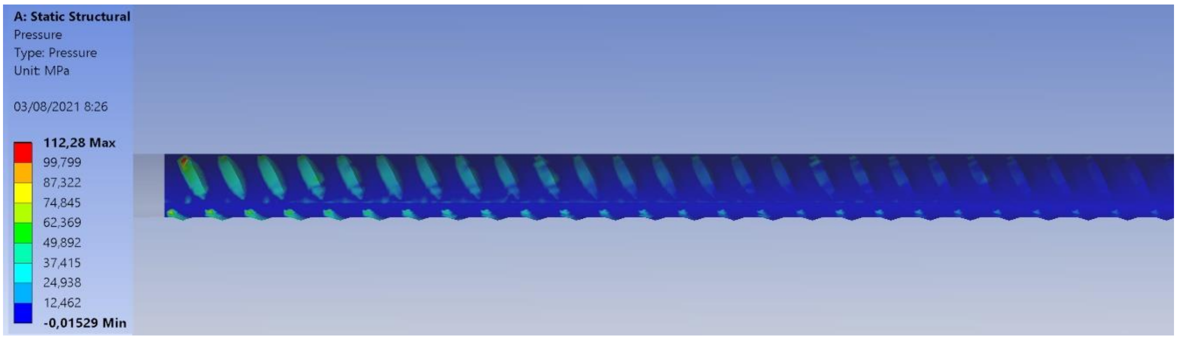

Fig. 8. Normal contact stress distribution when R reaches its final value.

4 Results

The results obtained in the first set of 40 simulations are presented in Table 1 below. The results are given in terms of force *R* (Table 1) as described in the previous section. The first set is composed of samples in which only one of the geometrical parameters, *Wc*, *We*, *B*, *Bf* or *hr* varies while the other parameters are set at a medium value. Three samples (samples number 12, 20 and 37) have been eliminated from the table for giving atypical results.

Sample number	*Wc* (mm)	*We* (mm)	*B* (^{0})	*Bf* (^{0})	*hr* (mm)	*R* (N)
1	1					20.309
2	1.5					20.314
3	2					20.347
4	2.5	2.5	35	67.5	0.45	20.358
5	3					20.385
6	3.5					20.395
7	4					20.413
8			75			20.357
9			70			20.364
10			65			20.361
11	2.5	2.5	60	67.5	0.45	20.358
13			50			20.362
14			45			20.366
15			40			20.333
16			35			20.361
17					0.15	20.357
18					0.25	20.347
19	2.5	2.5	35	67.5	0.35	20.354
21					0.55	20.358
22					0.65	20.355
23					0.75	20.360
24				45		20.393
25				50		20.382
26	2.5	2.5	35	55	0.45	20.351
27				60		20.352
28				65		20.353
29				70		20.352

30				75		20.355
31				80		20.356
32				85		20.357
33				90		20.364
34	2.5	1	35	67.5	0.45	20.363
35		1.5				20.360
36		2				20.317
38		3				20.294
39		3.5				20.330
40		4				20.358

Table 1. Values of the parameters *Wc*, *We*, *B*, *Bf*, and *hr* for the samples analysed in the first set and the corresponding force *R* obtained from calculations.

Based on the Pearson product-moment correlation matrix [55,56] where the contribution coefficient of each parameter in the value of *R* is identified (Table 2), it can be concluded that in the particular boundary conditions imposed on the samples in this research (prism with 12x12 mm^2 section and three longitudinal prism faces fixed), the most influential parameters in bonding are *hr*, *Wc*, and *B* in that order of importance.

	Wc	*We*	*B*	*Bf*	*hr*	*R*
Wc	1					
We	0	1				
B	0	0	1			
Bf	0	0	0	1		
Hr	0	0	0	0	1	
R	0.56	0.03	-0.11	0.07	0.74	1

Table 2. Pearson-Product product-moment correlation coefficient obtained for geometrical parameters and force R (N) for samples embedded in 12x12 mm^2 section prisms with 3 fixed longitudinal faces.

A multiple linear regression analysis of the results in Table 1 leads to the expression of *R* as follows:

$$R = 20.1389 + 0.0366 \cdot Wc + 0.0023 \cdot We + 0.0002 \cdot B + 0.0003 \cdot Bf + 0.2578 \cdot hr \qquad \text{[Eq. 9]}$$

This regression analysis exhibits 0.8721 a coefficient of R^2 determination, and a statistical P-value under 5%. It is therefore highly reliable. Apart from these data, the reliability of Equation 9 is ensured by means of a second set of Finite Element analysis. In this second set, composed of another 27 simulations, all values of geometrical parameters *Wc, We, B, Bf,* and *hr* range simultaneously. The geometrical parameters, as well as the force *R* obtained for each sample are compared with the value of *R* as predicted by Equation 9. The comparison confirms the accuracy of the results obtained from Equation 9, thereby allowing working with this equation (Table 3, Fig. 9).

Sample number	Wc (mm)	We (mm)	B (^{0})	Bf (^{0})	h (mm)	R (N)	$R_{predicted}$ (N)	Ratio (‰) $\frac{R_{predicted}-R}{R}$
41	1	1	75	45	0.15	20.260	20.211	-2.40
42	1.5	1.5	68.3	52.5	0.25	20.240	20.260	1.00
43	2	2	61.7	60	0.35	20.307	20.309	0.10
44	2.5	2.5	55	67.5	0.45	20.360	20.358	-0.10
45	3	3	48.4	75	0.55	20.434	20.407	-1.33
46	3.5	3.5	41.7	82.5	0.65	20.532	20.456	-3.72
47	4	4	35	90	0.75	20.654	20.505	-7.23
48	4	1	35	45	0.75	20.511	20.485	-1.26
49	1	2.5	35	45	0.45	20.327	20.302	-1.25
50	2.5	4	75	67.5	0.75	20.445	20.434	-0.53
51	1	4	55	90	0.75	20.367	20.390	1.14
52	2.5	1	35	45	0.15	20.239	20.277	1.81
53	4	2.5	75	90	0.45	20.399	20.414	0.76
54	1	1.5	61.7	67.5	0.55	20.302	20.325	1.13
55	1.5	2	55	75	0.65	20.361	20.374	0.63
56	2	2.5	48.4	82.5	0.75	20.440	20.423	-1.04
57	2.5	3	41.7	90	0.15	20.489	20.291	-9.66
58	3	3.5	35	45	0.25	20.333	20.325	-0.37
59	3.5	4	75	52.5	0.35	20.352	20.363	0.56
60	4	1	68.3	60	0.45	20.356	20.404	2.37
61	4	3.5	48.4	67.5	0.35	20.410	20.391	-0.93
62	3.5	3	55	60	0.25	20.488	20.342	-7.12
63	3	2.5	61.7	52.5	0.15	20.298	20.293	-0.24
64	2.5	2	68.3	45	0.75	20.386	20.425	1.90
65	2	1.5	75	90	0.65	20.363	20.391	1.35
66	1.5	1	35	82.5	0.55	20.396	20.353	-2.13
67	1	4	41.7	75	0.45	20.292	20.312	0.98

Table 3. Values of the parameters *Wc*, *We*, *B*, *Bf*, and *hr* for the 27 samples analysed in the second set, values for force *R* obtained from the calculations, values for force *R* predicted by Eq. 9, and ratio of the two values of force *R* for each sample.

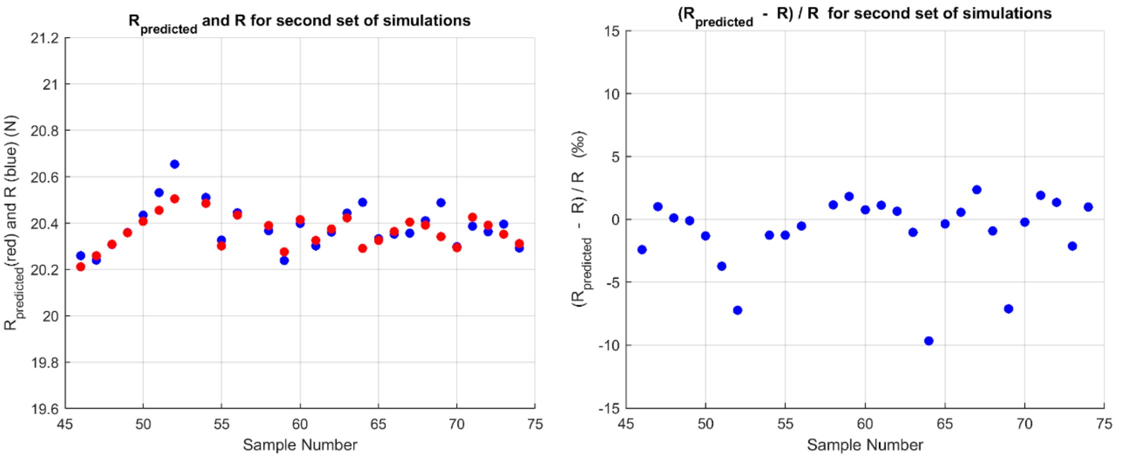

Fig. 9. Chart depicting the values of *R* (N) obtained in the second set of 27 simulations (in blue) and *R* (N) predicted by Equation 9 (in red) (left-hand side) and ratio $\frac{R_{predicted}-R}{R}$ (‰) (right-hand side).

To extend this research to a larger set of samples, the values of force *R* corresponding to a third set of 5,825 samples is obtained through Equation 9. The shape of these samples respond to the combination of geometrical parameters by ranging their values in steps: *Wc*, from 1.0 mm to 4 mm in 6 steps; *We*, from 1.0 mm to 4 mm, in 6 steps; *B*, from 35^0 to 75^0, in 4 steps; *Bf*, from 45^0 to 90^0, in 5 steps; *hr*, from 0.15 mm to 0.75 mm, in 6 steps. Although 8,575 possible combinations of values are numerically possible, only 5,825 of these combinations are geometrically possible. For all these samples, the parameterisation carried out by Grasshopper and Anemone has enabled the values to be obtained of: *Vr,* rib volume; *Sr,* rib external surface; and *Lr,* rib axis length. Among *Vr*, *Sr* and *Lr,* rib volume *Vr* has been adopted as the key parameter for the rib shape optimisation. From an economical point of view, volume, and therefore weight, is a decisive parameter when considering the financial feasibility of the rebars. Not only is rib volume directly linked with rib weight, but it also presents clear correlation with the value of force *R*. According to Pearson's correlation matrix [55,56], force *R* presents 96% correlation with rib volume, 83.0% with rib external surface, and only 23% with rib axis length.

The scatter graph of rib volume *Vr* and force *R* facilitates the identification of the samples that have produced the best and worst results in this research over the set of 5825 samples (Fig. 10). The diagram shows the values of *R* attained by ribs with a certain volume, and hence the lower band of the graph is considered as the worst-result set of samples (red), whereas the best-result set of samples is selected from among the points in the upper band (green). Both sets have been defined as bands with similar thicknesses. Finally, 272 samples compose the best-result set of samples.

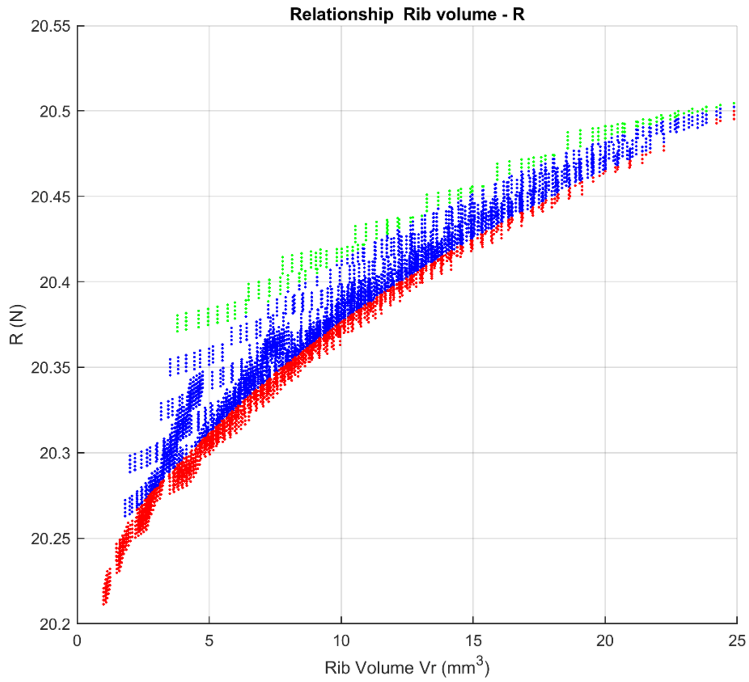

Fig. 10. Scatter plot representing force *R* in function of rib volume *Vr* for the 5,825 models analysed. Samples in the set of worst results depicted in red. Samples in the set of best results depicted in green.

Even though samples representing the best-result set and the worst-result set have been chosen with basis on a highly reliable equation (Eq. 9), a new verification has been carried out by means of a new set of Finite Elements calculations. To this end, two samples in the best-result set (samples 15 and 5012), representing ribs with low and high volume have been chosen. Two samples belonging to the worst-result set (samples 1276 and 4799) equipped with ribs which volume is similar to those selected from the best-result set have been also introduced in this verification (Fig. 11). Thus, four samples: sample 15 (*Wc*, 1 mm; *We*, 1 mm; *B*, 35º; *Bf*, 63º; *hr*, 0.75 mm), sample 1276 (*Wc*, 2 mm; *We*, 3 mm; *B*, 75º; *Bf*, 45º; *hr*, 0.25 mm), sample 4799 (*Wc*, 3.5 mm; *We*, 4 mm; *B*, 75º; *Bf*, 90º; *hr*, 0.65 mm) and sample 5012 (*Wc*, 4 mm; *We*, 2.5 mm; *B*, 35º; *Bf*, 45º; *hr*, 0.75 mm) have been analyzed up to failure. Figure 12 represents the value of the force R (N) transmitted to the hydraulic medium as a function of the longitudinal displacement applied to the sample.

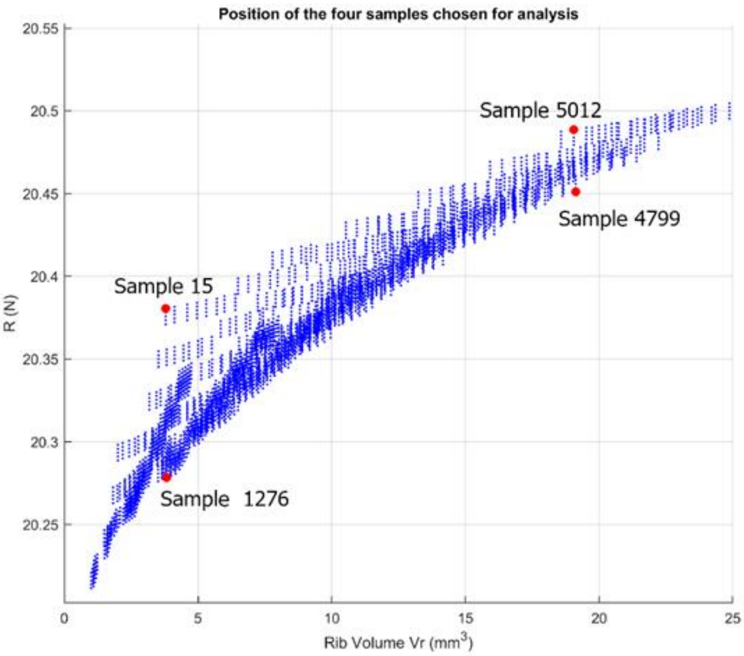

Fig. 11. Depiction of samples chosen to be analysed up to failure inside the scatter plot representing force *R* in function of rib volume *Vr* for the 5,825 samples

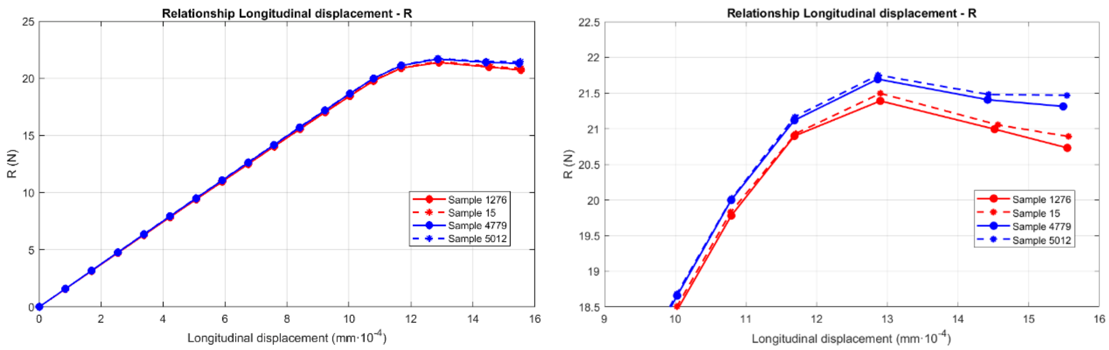

Fig. 12. Chart depicting the values of the force R (N) transmitted to the hydraulic medium as a function of the longitudinal displacement applied to the samples 15, 1276, 4799 and 5012: complete curves (left hand side) and detail of the failure area (right hand side). Dashed lines representing samples in the best-result set, continuous lines representing samples in the worst-result set. Red lines representing samples which ribs have low volume. Blue lines representing samples which ribs have high volume.

As expected according to Figure 11, best result in terms of force *R* is this attained by sample 5012 (21.752 N). In comparison with the sample 4799 (21.695 N), both with the same rib volume, sample 5012 implies

2.6% of improvement with respect to 4799. Analogously, the percentage of improvement of sample 15 (21.495 N) with respect of sample 1276 (21.389 N) is 5%. As position of points in Figure 11 predicted, sample 4799 (among the worst-result set) has attained a higher value of the force R than sample 15 (among the best-result set).

Contrarily, sample number 15 is more effective since its volume is sensibly lower, as Figure 13 demonstrates. Figure 13 that which represents the ratio *R/Vr* in function of the longitudinal displacement applied to samples, depicts clearly how samples in the best-result set are more efficient than those in the worst-result set, since are able to attain a higher value of force *R* with lower rib volume *Vr*.

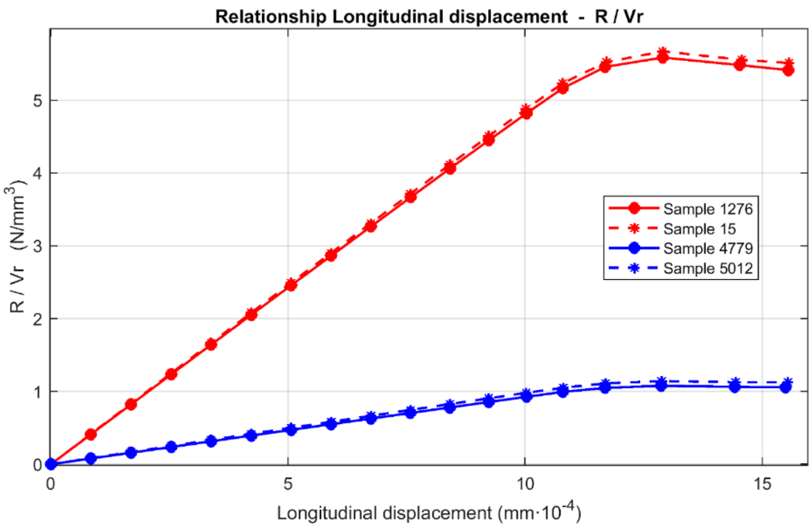

Fig. 13. Chart depicting the values of the rate between the force *R* (N) and de rib volume *Vr* as a function of the longitudinal displacement applied to the samples 15, 1276, 4799 and 5012. Dashed lines representing samples in the best-result set, continuous lines representing samples in the worst-result set. Blue lines representing samples which ribs have high volume. Red lines representing samples which ribs have low volume

5 Discussion

This section includes the discussion regarding the values of geometrical parameters and the combination of geometrical parameters defining ribs that positively influence the bonding behaviour of samples with diameter of 5 mm and three ribs, embedded in prisms with a 12x12 mm cross-section with 3 fixed longitudinal faces. To this end, the sets of the best and worst results of samples (Fig. 10) are analysed in search of common characteristics that can be related to this feature. The percentage of samples where certain values of the geometrical parameters *Wc*, *We*, *B*, *Bf*, and *hr* are present in the best and the worst result sets are therefore calculated (Table 4).

Wc (mm)	1.0	1.5	2.0	2.5	3.0	3.5	4.0
Percentage of the geometrical parameter in the best-result set	14.34	11.76	19.12	12.13	9.19	8.82	24.64
Percentage of the geometrical parameter in the worst-result set (%)	6.62	7.20	28.73	25.04	17.50	10.31	4.60
We (mm)	1.0	1.5	2.0	2.5	3.0	3.5	4.0
Percentage of the geometrical parameter in the best-result set (%)	13.60	12.50	22.43	17.65	14.71	10.66	8.45
Percentage of the geometrical parameter in the worst-result set (%)	6.56	7.25	8.23	12.21	16.81	21.59	27.35
B (º)	35	45	55	65	75	-	-
Percentage of the geometrical parameter in the best-result set	32.72	26.10	18.75	13.24	9.19	-	-
Percentage of the geometrical parameter in the worst-result set (%)	9.15	13.64	19.00	25.79	32.42	-	-
Bf (º)	45	54	63	72	81	90	-
Percentage of the geometrical parameter in the best-result set	38.24	20.22	13.97	10.66	8.82	8.09	-
Percentage of the geometrical parameter in the worst-result set (%)	13.64	16.35	17.16	17.85	18.25	16.75	-
hr (mm)	0.15	0.25	0.35	0.45	0.55	0.65	0.75
Percentage of the geometrical parameter in the best-result set	0	0	0	0	0	0.37	99.63
Percentage of the geometrical parameter in the worst-result set (%)	15.89	24.01	23.32	20.55	11.51	3.86	0.86

Table 4. Percentage of geometrical parameters in the best-result and worst-result sets of samples.

The most relevant parameter is undoubtedly the rib height *hr*: 100% of the ribs in the best-result set present rib height over 0.65 mm, this is, the highest possible values. In contrast, the lowest possible values of *hr* (under 0.35 mm) gather more than 60% of results. Although *hr* contributes positively towards the improvement of the results, an increase in this parameter also increases rib volume, making the efficiency of the rib rapidly decrease. Therefore, results in the worst-result set are more disperse than in the best-result set.

The angle *B* between the rib axis and that of the rebar is also a key parameter. Its importance is clear since in 58.82% of ribs in the best-result set, *B* is under 45º. In contrast, 58.21% of the ribs in the worst-result set present the highest values of this angle (over 65º). It is therefore easy to conclude that low values of the angle *B* favour bonding in this type of rebars.

Rib face angle *Bf* also presents a tendency to be low and high in the best-result and worst-result sets, respectively. In the best-result set, 58.46 % of the samples are obtained with 45º and 54º as the *Bf* angle, while the results in the worst-result set are disperse. Although *Bf* hardly influence the value of force *R* (Table 2), it is directly linked with the rib volume. As occurs with *hr*, an increase in this parameter leads to bulk ribs in which their efficiency rapidly decreases.

The importance of rib width remains unclear. Despite the fact that it constitutes one of the parameters with the most influence on *R* (Table 2), the percentages of results are scattered. In wide ribs, especially when *hr* is high, rib volume increases quickly, which easily leads to a non-efficient rib shape. This points towards the conclusion that increasing rib widths is of no interest. It is preferable to maintain these parameters in mid-range, largely to prevent geometrical incompatibility problems with a *Bf* of 45º, whose positive influence on the results has been demonstrated.

The relationship between certain parameters deserves special attention. From the rib plan, no clear conclusions can be extracted regarding the ratio between central and extremity widths. Apparently, the best results have been obtained in ribs wider in the centre than in the extremities, while the best results have been obtained in ribs in which occur exactly the opposite. Despite this fact, the percentage are quite scattered, what prevents any conclusion from being drawn (Table 5)

Relationship of the parameters *Wc* and *We*	Wc > We	Wc = We	Wc < We
Percentage of samples in the best-result set meeting the criteria (%)	43.75	27.57	28.68
Percentage of samples in the worst-result set meeting the criteria (%)	15.03	23.43	61.54

Table 5. Percentage of samples in best-result and worst-result sets where a specific relationship between *Wc* and *We* is present.

The relationships among parameters confirm the conclusions that have been already drawn. Among the best possible combinations are low values of angle *Bf* with high values of *hr* (72.45%) and low values of angle *B* with high values of *hr*. On the contrary, the worst combinations of parameters involve high values of *B* and *Bf* and high values of *B* with low values of *hr* (Table 6).

Range of the parameters *Bf* and *hr*	*Bf* > 67.5º *hr* > 0.4 mm	*Bf* > 67.5º *hr* < 0.4 mm	*Bf* < 67.5º *hr* > 0.4 mm	*Bf* < 67.5º *hr* < 0.4 mm
Percentage of samples in the best-result set meeting the criteria (%)	27.25	0	72.45	0
Percentage of samples in the worst-result set meeting the criteria (%)	25.45	27.40	11.34	35.81
Range of the parameters *B* and *hr*	*B* > 50º *hr* > 0.4 mm	*B* >50º *hr* < 0.4 mm	*B* < 50º *hr* > 0.4 mm	*B* < 50º *hr* < 0.4 mm
Percentage of samples in the best-result set meeting the criteria (%)	41.18	0	58.82	0
Percentage of samples in the worst-result set meeting the criteria (%)	32.01	45.19	4.78	18.02
Range of the parameters *Bf* and *B*	*Bf* > 67.5º *B* >50º	*Bf* > 67.5º *B* < 50º	*Bf* < 67.5º *B* > 50º	*Bf* < 67.5º *B* < 50º
Percentage of samples in the best-result set meeting the criteria (%)	9.93	17.65	31.25	41.18
Percentage of samples in the worst-result set meeting the criteria (%)	41.67	11.28	35.64	11.51
Range of the parameters *Wc* and *hr*	*Wc* > 2.25 mm *hr* > 0.4 mm	*Wc* > 2.25 mm *hr* < 0.4	*Wc* < 2.25 mm *hr* > 0.4	*Wc* < 2.25 mm *hr* < 0.4 mm
Percentage of samples in the best-result set meeting the criteria (%)	54.78	0	45.22	0
Percentage of samples in the worst-result set meeting the criteria (%)	30.97	26.48	5.82	36.73

Table 6. Percentage of geometrical parameters in the best-result and worst-result sets of samples.

Finally, among the samples in the best-result set (Fig. 10), the relationship between reaction force *R* and rib volume *Vr* is established thought the tendency curve, presenting with R^2 fitting coefficient of 0.991 (Fig. 14):

$$R = 20.3502 + 0.00489 \cdot Vr + 0.00029 \cdot Vr^2 - 0.00001 \cdot Vr^3 \qquad \text{[Eq. 10]}$$

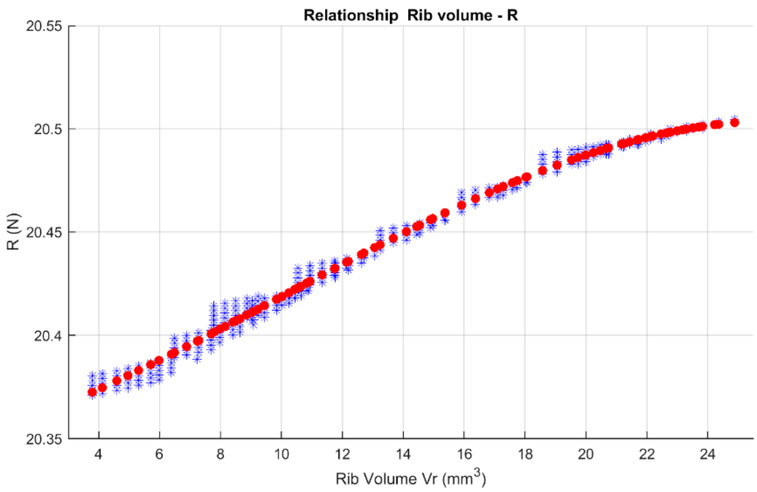

Fig. 14. Scatter graph representing values of force *R* (N) in function of rib volume *Vr* for the samples in the best-result set and tendency curve fitting this data.

This expression, which supposes the optimum relationship between rib volume *Vr* and reaction force *R*, together with Equation 9, which relates geometrical parameters *Wc*, *We*, *B*, *Bf*, and *hr* with the value of reaction force *R*, enable the establishment of the optimum relationship between rib *Vr* volume and the geometrical parameters used in this research:

$$0.0366 \cdot Wc + 0.0023 \cdot We + 0.0002 \cdot B + 0.0003 \cdot Bf + 0.2578 \cdot hr = 0.2113 + 0.00489 \cdot \mathrm{Vr} + 0.00029 \cdot \mathrm{Vr}^2 - 0.00001 \cdot \mathrm{Vr}^3 \quad \text{[Eq. 11]}$$

As a result of this research, Equation 11 establishes the relationship between the geometrical parameters of the rib and rib volume in order to attain an efficient rib under the particular conditions of this research.

6 Conclusions

This paper studies the most influential geometrical parameters of rib shape regarding bonding behaviour in small-diameter rebars employed in the reinforcement of masonry bed joints. To this end, 67 steel samples embedded in prisms of hydraulic material with a 12 mm x 12 mm cross-section are analysed using FEM. Samples consist of a central core in which a single row of ribs is attached, thereby preventing any influence of spacing between the ribs. The results are analysed in terms of the amount of force *R* required to displace the sample a certain distance from their initial position inside the prisms.

The Microplane model is employed to simulate the behaviour of a hydraulic medium. This model is especially suitable for the characterisation of the behaviour of quasi-brittle materials where non-linear stress-strain relations with brittle cracking are always present. A cohesive zone model is utilised to simulate the contact interface between the prisms and the samples. The results of the calculations are evaluated based on the force transmitted from the rebar to the grout.

The numerical quality correlation obtained between the geometrical parameters and the results of the calculations has enabled the results to be extrapolated to several iterations. Altogether, 5,825 samples are analysed by using the data obtained via the mathematical relationships established by means of regression analysis. The correlation matrix of the results in terms of R alongside the properties of rib surface, rib axis length, and rib volume shows that rib volume is the geometrical property that best matches the behaviour of the rib in the context of bonding. This fact diverges from the criteria of certain codes, in which bonding is evaluated though the transverse projection of the longitudinal section of the rib.

Regarding rib shape and according to the results obtained from the set of 5,825 samples, it can be stated that the most efficient ribs are those that present high rib height, low rib face angle and low angle between the rib and rebar axes. Concerning widths, narrow ribs are preferable despite the fact that the central width presents a significant relationship with the resulting force R when the rebar is subjected to the particular boundary conditions imposed in this research. The reason can be found in the link between the rib width and rib volume, which can lead to the attainment of a non-financially feasible rib. Finally, a mathematical relationship between geometrical parameters and rib volume is established in order to attain an efficient rib.

As further development of this research, suitable spacing between ribs must be introduced into the method for the rebar geometry to be fully optimised.

7 Funding

This research has been carried out under the project PGC2018-098185-A-I100, funded by: FEDER/Ministerio de Ciencia e Innovación-Agencia Estatal de Investigación of Spain.

8 References

[1] E. Rodríguez-Mayorga, E. Yanes-Bustamante, A. Sáez-Pérez, Analysis and diagnosis of the church of Santiago in Jerez de la Frontera (Spain), Inf. La Constr. 67 (2015). https://doi.org/10.3989/ic.15.030.

[2] E. Rodriguez-Mayorga, La rehabilitación del templo parroquial de Santiago Apóstol: anamnesis, diagnosis, terapia y control, PhD Thesis, University of Sevilla, 2011. http://fondosdigitales.us.es/tesis/tesis/2621/rehabilitacion-del-templo-parroquial-de-santiago-apostol-en-jerez-de-la-frontera-anamnesis-diagnosis-terapia-y-control/.

[3] D. V. Oliveira, R.A. Silva, E. Garbin, P.B. Lourenço, Strengthening of three-leaf stone masonry walls: An experimental research, Mater. Struct. Constr. 45 (2012) 1259–1276. https://doi.org/10.1617/s11527-012-9832-3.

[4] A. Anzani, G. Cardani, P. Condoleo, E. Garavaglia, A. Saisi, C. Tedeschi, C. Tiraboschi, M.R. Valluzzi, Understanding of historical masonry for conservation approaches: the contribution of Prof. Luigia Binda to research advancement, Mater. Struct. Constr. 51 (2018) 1–27. https://doi.org/10.1617/s11527-018-1254-4.

[5] M.R. Valluzzi, M. Salvalaggio, L. Sbrogiò, Repair and conservation of masonry structures, in: G.M. Bahman Ghiassi (Ed.), Numer. Model. Mason. Hist. Struct. From Theory to Appl., Woodhead Publishing - Elsevier, 2019: pp. 201–235. https://doi.org/10.1016/b978-0-08-102439-3.00006-3.

[6] M. Corradi, G. Castori, A. Borri, Repairing brickwork panels using titanium rods embedded in the mortar joints, Eng. Struct. 221 (2020) 111099. https://doi.org/10.1016/j.engstruct.2020.111099.

[7] B. Behera, R.P. Nanda, In-plane shear strengthening of brick masonry panel with geogrid reinforcement embedded in bed and bed-head joints mortar, Eng. Struct. 227 (2021) 111411. https://doi.org/10.1016/j.engstruct.2020.111411.

[8] M.R. Valluzzi, L. Binda, C. Modena, Mechanical behaviour of historic masonry structures strengthened by bed joints structural repointing, Constr. Build. Mater. 19 (2005) 63–73. https://doi.org/10.1016/j.conbuildmat.2004.04.036.

[9] L. Binda, C. Modena, A. Saisi, R. Tongini-Folli, M.R. Valluzzi, Bedjoint structual repointing of

historic masonry structures, in: J.L.D. P. H. Bischoff (Ed.), 9th Can. Mason. Symp., University of New Brunswick, Department of Civil Engineering, Frederickton, 2001.

[10] M. Candela, A. Borri, M. Corradi, L. Righetti, Effect of transversal steel connectors on the behavior of rubble stone-masonry walls: Two case studies in Italy, Brick Block Mason. Trends, Innov. Challenges - Proc. 16th Int. Brick Block Mason. Conf. IBMAC 2016. (2016) 2029–2038. https://doi.org/10.1201/b21889-252.

[11] S.A. Babatunde, Review of strengthening techniques for masonry using fiber reinforced polymers, Compos. Struct. 161 (2017) 246–255. https://doi.org/10.1016/j.compstruct.2016.10.132.

[12] M.R. Valluzzi, On the vulnerability of historical masonry structures: analysis and mitigation, Mater. Struct. Constr. 40 (2007) 723–743. https://doi.org/10.1617/s11527-006-9188-7.

[13] M. Molnár, O. Larsson Ivanov, Clay brick masonry facades with cracks caused by corroding bed joint reinforcement – Findings from field survey and laboratory study, Constr. Build. Mater. 125 (2016) 775–783. https://doi.org/10.1016/j.conbuildmat.2016.08.081.

[14] F. Ancio, E. Rodriguez-Mayorga, B. Hortigon, Analysis of the Main Aspects Affecting Bonding in Stainless Steel Rebars Embedded in a Hydraulic Medium, Metals (Basel). 11 (2021) Article number 786. https://doi.org/doi:10.3390/met11050786.

[15] ACI Committee 408, Bond and Development of Straight Reinforcing Bars in Tension Reported by ACI Committee 408, Aci 408-03. (2003) 1–49.

[16] CEn European Commitee for Standardization, EN 1992-2: Design of concrete structures, 1992.

[17] I.O. for Standardization, ISO 6935-2:2019 Preview Steel for the reinforcement of concrete. Part 2: Ribbed bars, 2015 (2019).

[18] A 615/A 615M – 12, Standard Specification for Deformed and Plain Carbon-Steel Bars for Concrete Reinforcement, Astm. (2012) 6. https://doi.org/10.1520/A0615.

[19] D. Darwin, E.K. Graham, Effect of deformation height and spacing on bond strength of reinforcing bars, ACI Mater. J. 90 (1993) 646–657. https://doi.org/10.14359/4459.

[20] J. Zuo, D. Darwin, Bond slip of high relative rib area bars under cyclic loading, ACI Struct. J. 97

(2000) 331–334. https://doi.org/10.14359/864.

[21] G. Metelli, G.A. Plizzari, Influence of the relative rib area on bond behaviour, Mag. Concr. Res. 66 (2014) 277–294. https://doi.org/10.1680/macr.13.00198.

[22] M.S. Lorrain, L.F. Caetano, B. V. Silva, L.E.S. Gomes, M.P. Barbosa, L.C.P. Silva Filho, Bond strength and rib geometry: A comparative study of the influence of deformation patterns on anchorage bond strength, 3rd Int. Fib Congr. Exhib. Inc. PCI Annu. Conv. Bridg. Conf. Think Glob. Build Locally, Proc. (2010).

[23] L.C.P. Silva Filho, B. Vale Silva, V.I. Dal Bosco, L.E.S. Gomes, M.P. Barbosa, M. Lorrain, Analysis of the influence of rebar geometry variations on bonding strength in the pull-out test, Bond Concr. 2012. 1-General (2012) 63–68. papers3://publication/uuid/A0125CCB-501F-4443-A798-F6B5D21E5B9B.

[24] O.C. Choi, S.Y. Yang, Bearing angle model for bond of reinforcing bars to concrete, 11th Int. Conf. Fract. 2005, ICF11. 2 (2005) 1393–1398.

[25] M.T. Barbosa, E. de S. Sánchez Filho, T.M. de Oliveira, W.J. dos Santos, Analysis of the relative rib area of reinforcing bars pull out tests, Mater. Res. 11 (2008). https://doi.org/DOI: 10.1590/S1516-14392008000400013.

[26] W. Tao, C. Chen, H. Jun, R. Ting, Effect of bolt rib spacing on load transfer mechanism, Int. J. Min. Sci. Technol. 27 (2017) 431–434. https://doi.org/10.1016/j.ijmst.2017.03.009.

[27] L.A. Lutz, P. Gergely, Mechanics of bond and slip of deformed bars in concrete, Am Concr. Inst J. Proc. 64 (1967) 711–721.

[28] H.C. Biscaia, S. Soares, Adherence prediction between ribbed steel rebars and concrete: A new perspective and comparison with codes, Structures. 25 (2020) 979–999. https://doi.org/10.1016/j.istruc.2020.04.019.

[29] C. B/517/8, BS EN 1881:2006 – Products and systems for the protection and repair of concrete structures – test methods – testing of anchoring products by pull-out method, BSI, 2006.

[30] BS EN 846-2:2000 - Methods of test for ancillary components for masonry - Part 2: Determination of bond strength of prefabricated bed joint reinforcement in mortar joints., 2000.

[31] B. Hortigón, J.M. Gallardo, E. Nieto, J.A. López, Elasto-plastic hardening models adjustment to ferritic, austenitic and austenoferritic Rebar, Rev. Metal. 53 (2017) e094. https://doi.org/http://dx.doi.org/10.3989/revmetalm.094.

[32] B. Hortigón, J.M. Gallardo, E.J. Nieto-García, J.A. López, Strain hardening exponent and strain at maximum stress: Steel rebar case, Constr. Build. Mater. 196 (2019). https://doi.org/10.1016/j.conbuildmat.2018.11.082.

[33] Z.P. Bažant, P.C. Prat, Microplane model for brittle-plastic material: II. verification, J. Eng. Mech. 114 (1988) 1689–1702. https://doi.org/10.1061/(ASCE)0733-9399(1988)114:10(1689).

[34] Z.P. Bažant, P.C. Prat, Microplane model for brittle-plastic material: I. Theory, J. Eng. Mech. 114 (1988) 1672–1688. https://doi.org/10.1061/(ASCE)0733-9399(1988)114:10(1672).

[35] F.C. Caner, Z.P. Bažant, Microplane model M4 for concrete. II: Algorithm and calibration, J. Eng. Mech. 126 (2000) 954–961. https://doi.org/10.1061/(ASCE)0733-9399(2000)126:9(954).

[36] G. Cusatis, X. Zhou, High-order microplane theory for quasi-brittle materials with multiple characteristic lengths, J. Eng. Mech. 140 (2014). https://doi.org/10.1061/(ASCE)EM.1943-7889.0000747.

[37] Z.P. Bažant, P.G. Gambarova, Crack shear in concrete: Crack band microplane model, J. Struct. Eng. (United States). 110 (1984) 2015–2035. https://doi.org/10.1061/(ASCE)0733-9445(1984)110:9(2015).

[38] I. Carol, M. Jirásek, Z. Bažant, A thermodynamically consistent approach to microplane theory Part I. Free energy and consistent microplane stresses, Int. J. Solids Struct. 38 (2001) 2921–2931. https://doi.org/10.1016/S0020-7683(00)00212-2.

[39] Z.P. Bažant, P. Gambarova, ROUGH CRACKS IN REINFORCED CONCRETE, ASCE J Struct Div. 106 (1980) 819–842.

[40] Z.P. Bažant, B.H. Oh, Microplane model for progressive fracture of concrete and rock, J. Eng. Mech. 111 (1985) 559–582. https://doi.org/10.1061/(ASCE)0733-9399(1985)111:4(559).

[41] I. Carol, P.C. Prat, Z.P. Bažant, New explicit microplane model for concrete: Theoretical aspects and numerical implementation, Int. J. Solids Struct. 29 (1992) 1173–1191.

https://doi.org/10.1016/0020-7683(92)90141-F.

[42] I. Carol, Z.P. Bažant, Damage and plasticity in microplane theory, Int. J. Solids Struct. 34 (1997) 3807–3835. https://doi.org/10.1016/S0020-7683(96)00238-7.

[43] J. Mazars, G. Pyaudier-Cabot, Continuum damage theory—application to concrete, J. Eng. Mech. 115 (1989) 345–365. https://doi.org/10.1061/(ASCE)0733-9399(1989)115:2(345).

[44] R.H.J. Peerlings, R. de Borst, W.A.M. Brekelmans, M.G.D. Geers, Gradient-enhanced damage modelling of concrete fracture, Mech. Cohesive-Frictional Mater. 3 (1998) 323–342. https://doi.org/10.1002/(SICI)1099-1484(1998100)3:4<323::AID-CFM51>3.0.CO;2-Z.

[45] M.G.D. Geers, R. De Borst, W.A.M. Brekelmans, R.H.J. Peerlings, Strain-based transient-gradient damage model for failure analyses, Comput. Methods Appl. Mech. Eng. 160 (1998) 133–153.

[46] J.H.P. de Vree, W.A.M. Brekelmans, M.A.J. van Gils, Comparison of nonlocal approaches in continuum damage mechanics, Comput. Struct. 55 (1995) 581–588. https://doi.org/10.1016/0045-7949(94)00501-S.

[47] J.H.P. de Vree, W.A.M. Brekelmans, M.A.J. file:///E:/Pos.-D..-0045794994400501S-main. pd. van Gils, Comparison of nonlocal approaches in continuum damage mechanics, Comput. Struct. 55 (1995) 581–588. https://doi.org/10.1016/0045-7949(94)00501-S.

[48] I. Zreid, M. Kaliske, A gradient enhanced plasticity–damage microplane model for concrete, Comput. Mech. (2018). https://doi.org/10.1007/s00466-018-1561-1.

[49] L. Binda, A. Fontana, G. Frigerio, Mechanical behaviour of brick masonries derived from unit and mortar characteristics, in: J.W.T. Courcy (Ed.), 8th Int. Brick Block Mason. Conf. IB2MAC 1988, Dublin (Ireland), 1988: pp. 205–216.

[50] P. Cornetti, M. Muñoz-Reja, A. Sapora, A. Carpinteri, Finite fracture mechanics and cohesive crack model: Weight functions vs. cohesive laws, Int. J. Solids Struct. 156–157 (2019) 126–136. https://doi.org/10.1016/j.ijsolstr.2018.08.003.

[51] J.I. Gisbert, D. Bru, A. Gonzalez, S. Ivorra, Masonry micromodels using high order 3D elements, in: Procedia Struct. Integr., 2018. https://doi.org/10.1016/j.prostr.2018.11.055.

[52] L. Chiriatti, H. Mercado-Mendoza, K.L. Apedo, C. Fond, F. Feugeas, A study of bond between steel rebar and concrete under a friction-based approach, Cem. Concr. Res. (2019). https://doi.org/10.1016/j.cemconres.2019.03.019.

[53] M.T.G. Barbosa, E. de S. Sánchez Filho, T.M. de Oliveira, W.J. dos Santos, Analysis of the relative rib area of reinforcing bars pull out tests, Mater. Res. 11 (2009) 453–457. https://doi.org/10.1590/s1516-14392008000400013.

[54] S. Mehendale, A. Bambole, S. Raghunath, Desarrollo de un pseudo-elemento de interfaz para el modelado de mampostería de ladrillo reforzado, ALCONPAT. 7 (2017) 73–86. https://doi.org/http://dx.doi.org/10.21041/ra.v7i1.147.

[55] G.D. Ashkezari, F. Fotouhi, M. Razmara, Experimental relationships between steel fiber volume fraction and mechanical properties of ultra-high performance fiber-reinforced concrete, J. Build. Eng. 32 (2020) 101613. https://doi.org/10.1016/j.jobe.2020.101613.

[56] K. Pearson, VII. Note on regression and inheritance in the case of two parents, R. Soc. Publ. 58 (1895) 240–242. https://doi.org/https://doi.org/10.1098/rspl.1895.0041.